Supporting Information for "Reduction in the Tropical High Cloud Fraction in Response to an Indirect Weakening of the Hadley Cell"

S. R. Monisha Natchiar[1], Mark J Webb[2], F Hugo Lambert[1], Geoffrey K Vallis[1], Cyril J Morcrette[1,2], Christopher E. Holloway[3], Denis E. Sergeev[4]

[1]Department of Mathematics and Statistics, University of Exeter, Exeter EX4 4QE, UK

[2]Met Office, FitzRoy Road, Exeter EX1 3PB, UK

[3]Department of Meteorology, University of Reading, Reading RG6 6BB, UK

[4]Department of Physics and Astronomy, University of Exeter, Exeter, EX4 4QL, UK

Contents of this file

1. Figures S1 to S12

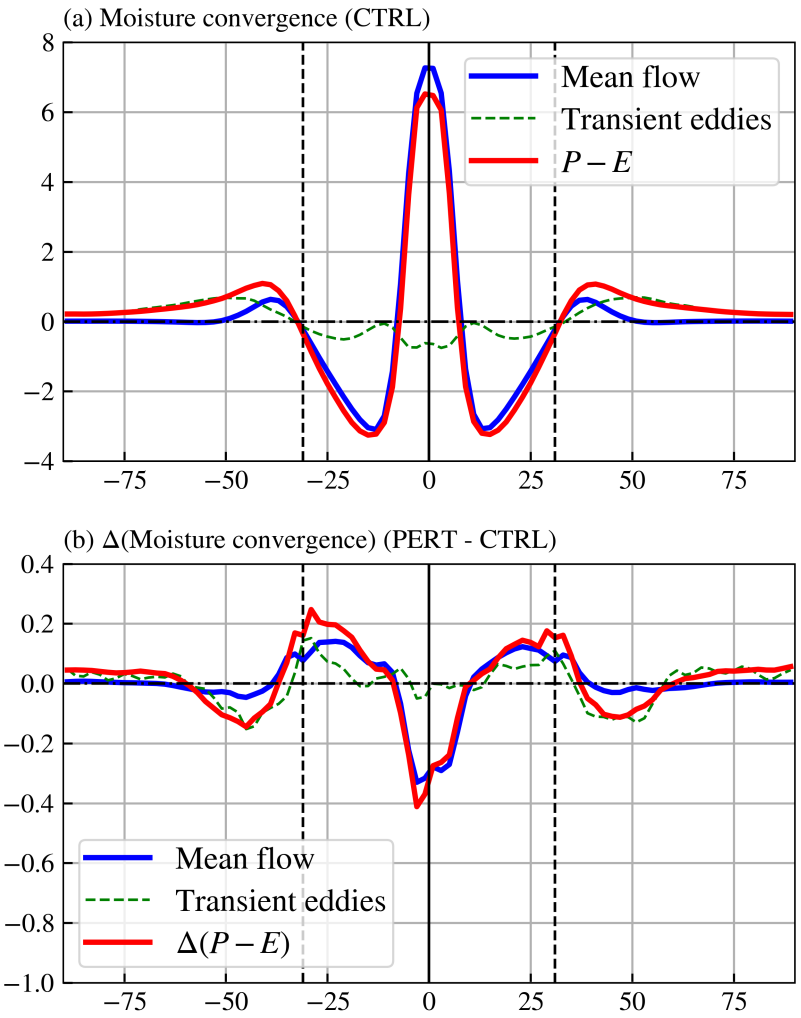

Figure S1. Moisture convergence by the mean flow and the transient eddies in the control simulation with PC2 cloud scheme and GR mass-flux convection scheme is plotted in (a), while the difference in moisture convergence between the perturbed and control simulations is plotted in (b) that shows a decrease in the mean moisture convergence in the deep tropics. The vertically integrated moisture convergence by the mean flow is computed as $\nabla_h \cdot \int_0^{z_t} \bar{\rho}\bar{q}\bar{\mathbf{v}}_h \, \mathrm{d}z$, where $\bar{\mathbf{v}}_h$ is the time-mean horizontal velocity vector, $\bar{q}$ is the time-mean specific humidity, and z_t denotes the top-of-atmosphere height. Similarly, the moisture convergence by the transient eddies is given by $\nabla_h \cdot \int_0^{z_t} \bar{\rho}\overline{q'\mathbf{v}'_h} \, \mathrm{d}z$, where prime ($'$) denotes the respective transient eddy quantities. Note that $P-E$ approximately balances the sum of moisture convergence terms due to the mean flow and transient eddies.

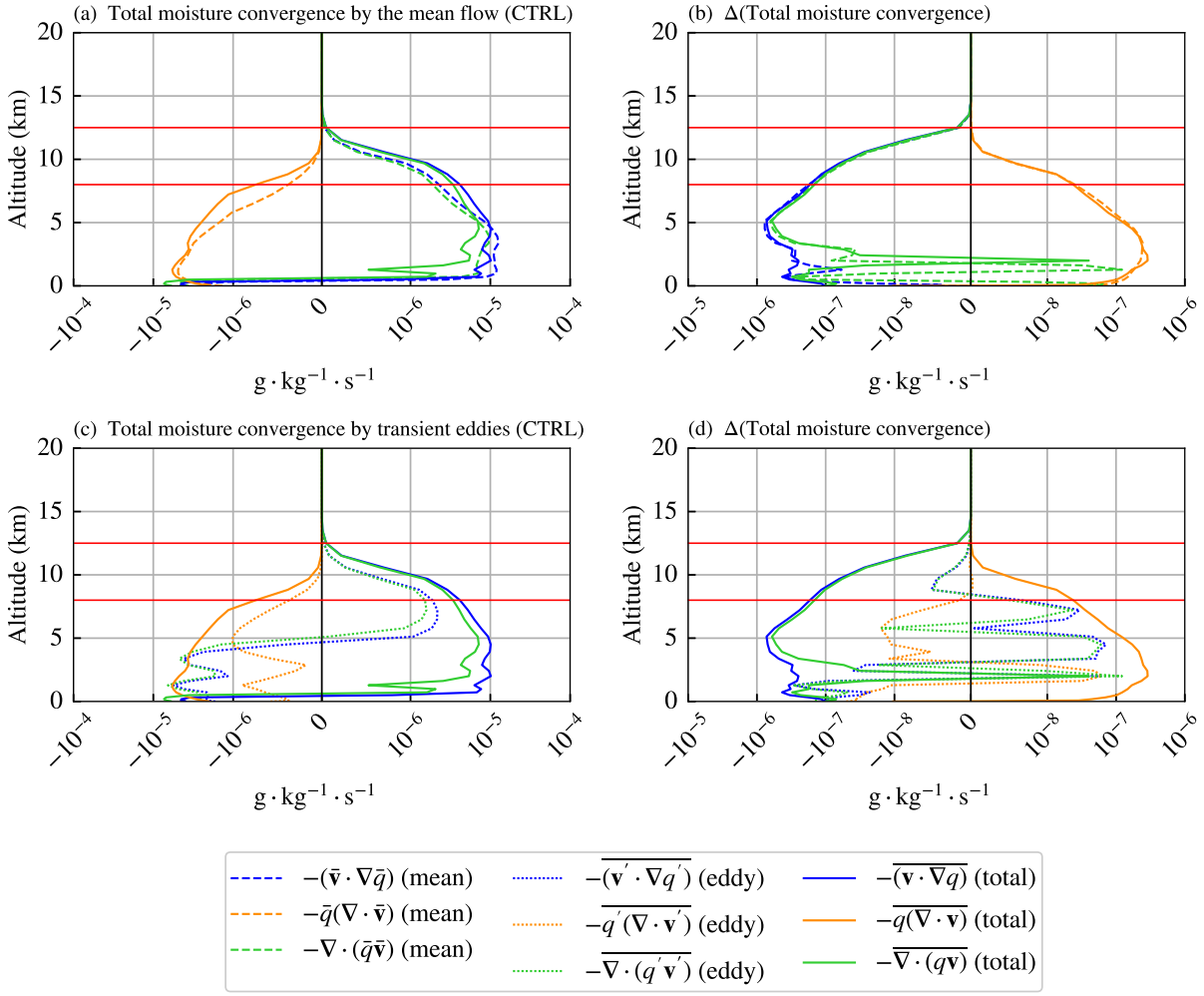

Figure S2. Moisture convergence by the mean flow (dashed curves) in the control simulation is shown in (a) and their response to extratropical warming is shown in (b). Similarly, the moisture convergence by the transient eddies (dotted curves) in the control is shown in (c) and their response in (d). Both simulations are run with the PC2 cloud scheme and GR mass-flux convection scheme. The solid curves indicate the total moisture convergence given by the sum of mean flow and transient eddy terms. The moisture convergence by the mean flow and transient eddies are further decomposed into advection (blue) and flow convergence terms (orange), with their sum represented by green curves. See Appendix A for more details on the derivation. The region of investigation is bounded by horizontal solid red lines; each of the terms plotted are averaged quantities over the tropical ascent region.

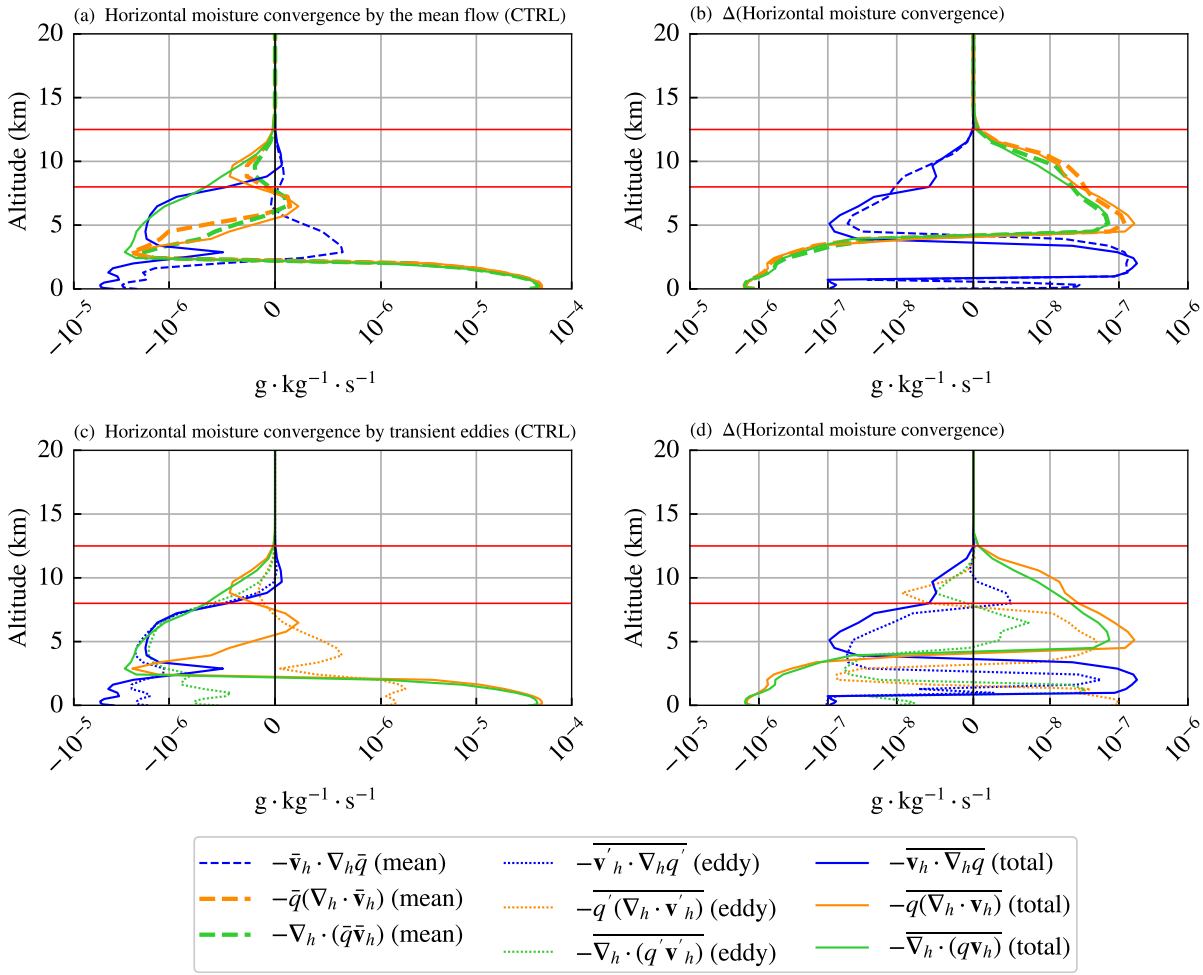

Figure S3. As in figure S2, but for the horizontal moisture convergence terms by the mean flow (dashed curves) in (a) and their response in (b), with the transient eddy components (dotted curves) in the control and the response plotted in (c) and (d), respectively. Note that while the horizontal moisture convergence predominantly influences the boundary layer transport of moisture, it does not contribute significantly to the upper-tropospheric moisture convergence, in comparison to vertical moisture convergence.

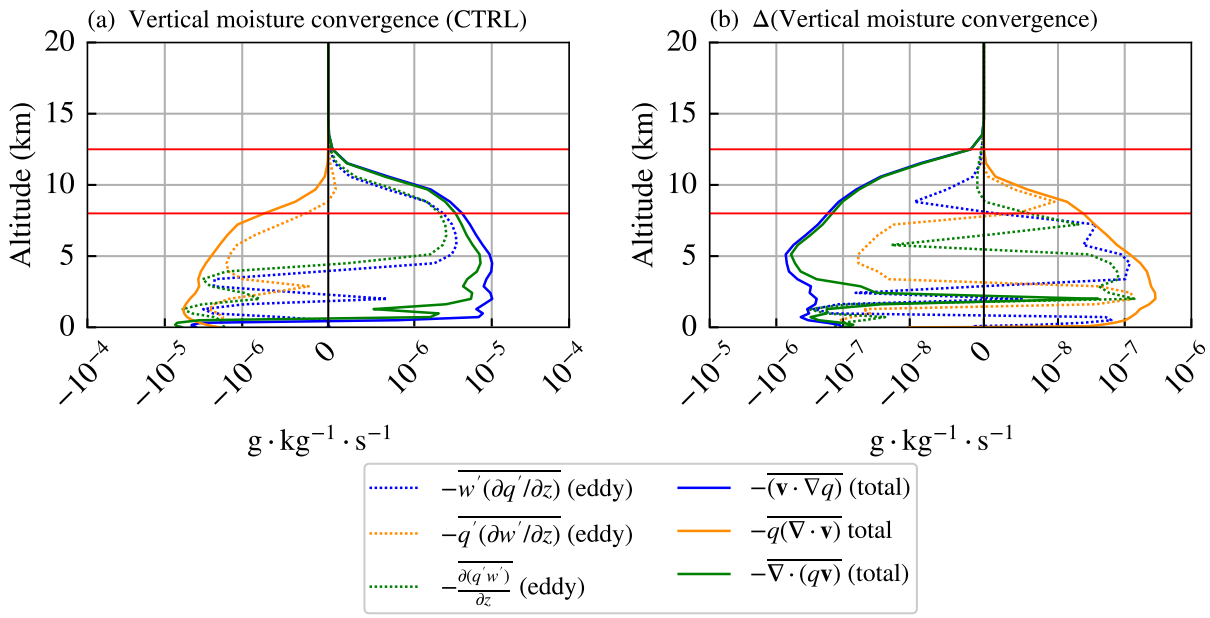

Figure S4. Vertical moisture convergence by the transient eddies (dotted curves) and the total moisture convergence terms (solid curves) are plotted in the control simulation in (a) and their response to extratropical warming in (b). Although transient eddies transport moisture into the deep tropics via vertical advection in the control, their response to extratropical warming is not significant in the region of interest compared to the changes in the mean vertical advection of moisture.

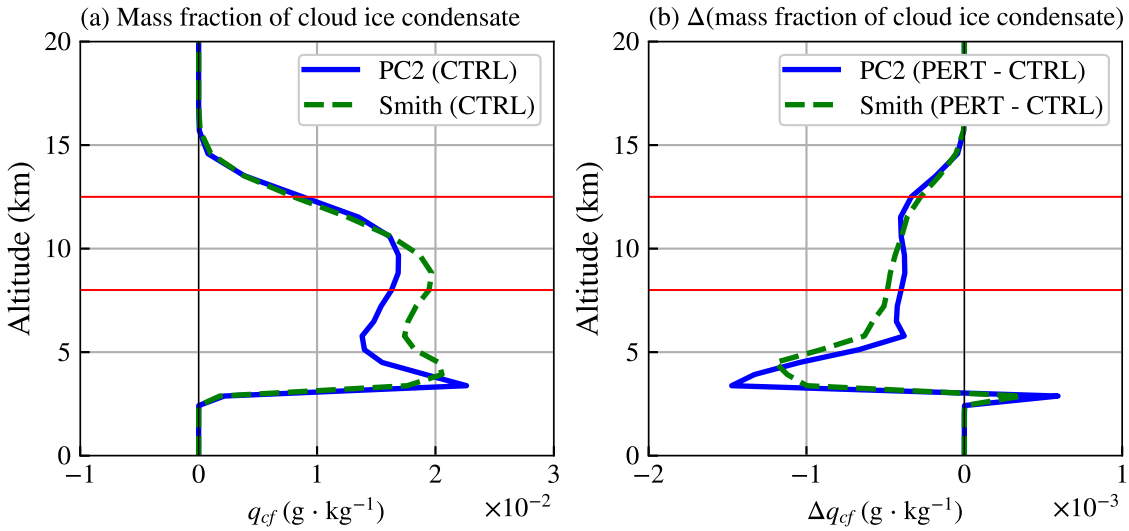

Figure S5. Vertical profiles of the mass fraction of ice cloud condensates (q_{cf}) in the control simulations (a) and the response to extratropical surface warming (b) are shown for both prognostic and diagnostic cloud schemes in the tropical ascent region. Both cloud schemes show a reduction in the ice cloud condensate amounts in the tropical ascent region. Red lines demarcate the region of interest (i.e., tropical upper-troposphere).

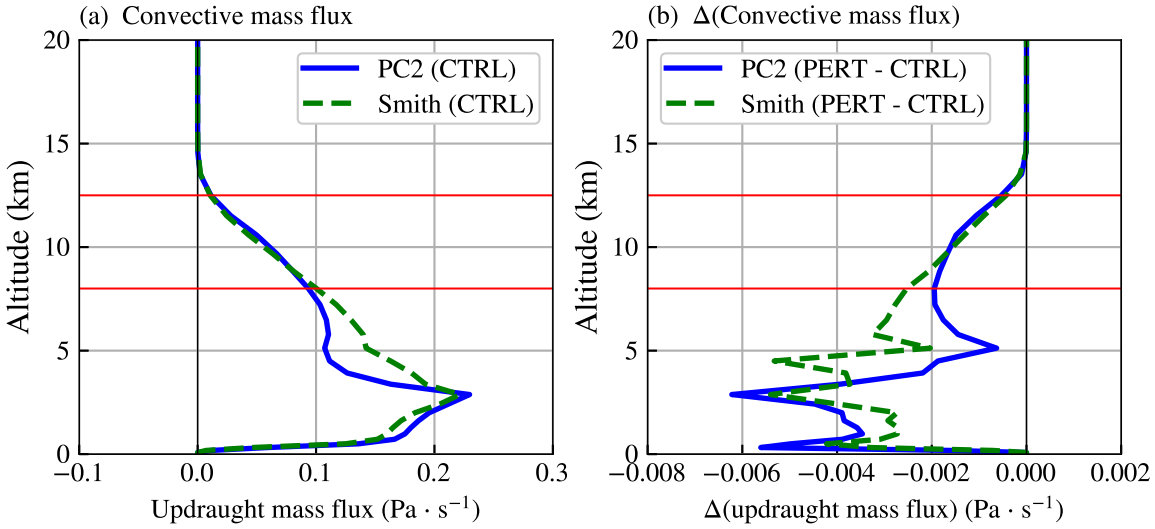

Figure S6. Vertical profiles of the updraft mass flux in the control simulation (a) and the response to extratropical warming (b) are plotted for two different cloud schemes. A decrease in the convective mass flux occurs as a result of a weakened Hadley circulation as is expected.

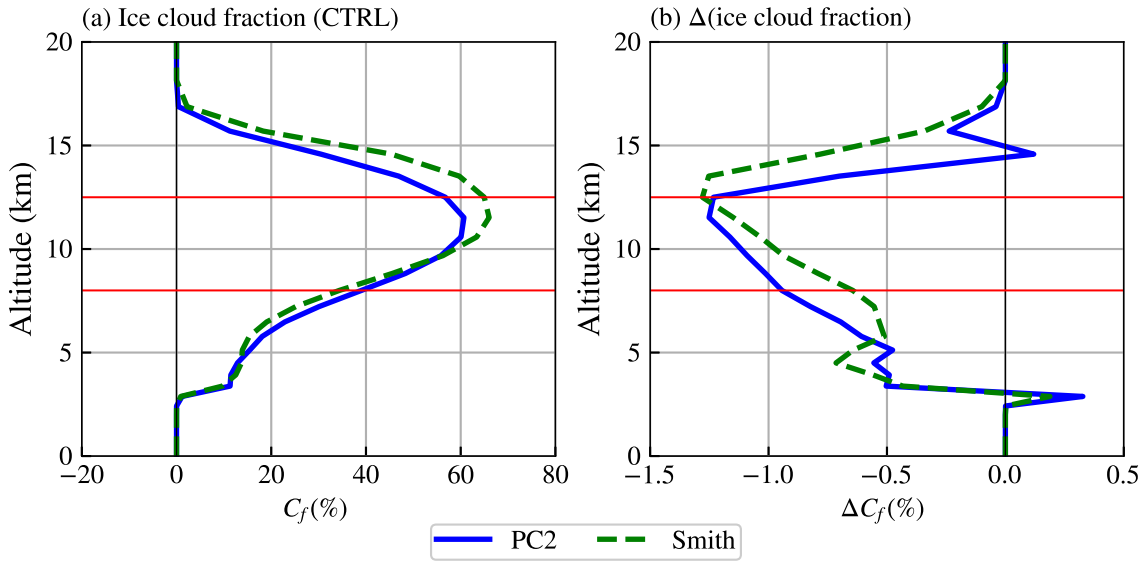

Figure S7. Vertical profiles of the ice cloud fraction (C_f) in the control simulation (a) and the difference between perturbed and control simulations (b) are plotted for two different cloud schemes. A maximum decrease in the ice cloud fraction of at least 1% can be observed at around 11.5 km where the ice cloud fraction peaks in the control simulation.

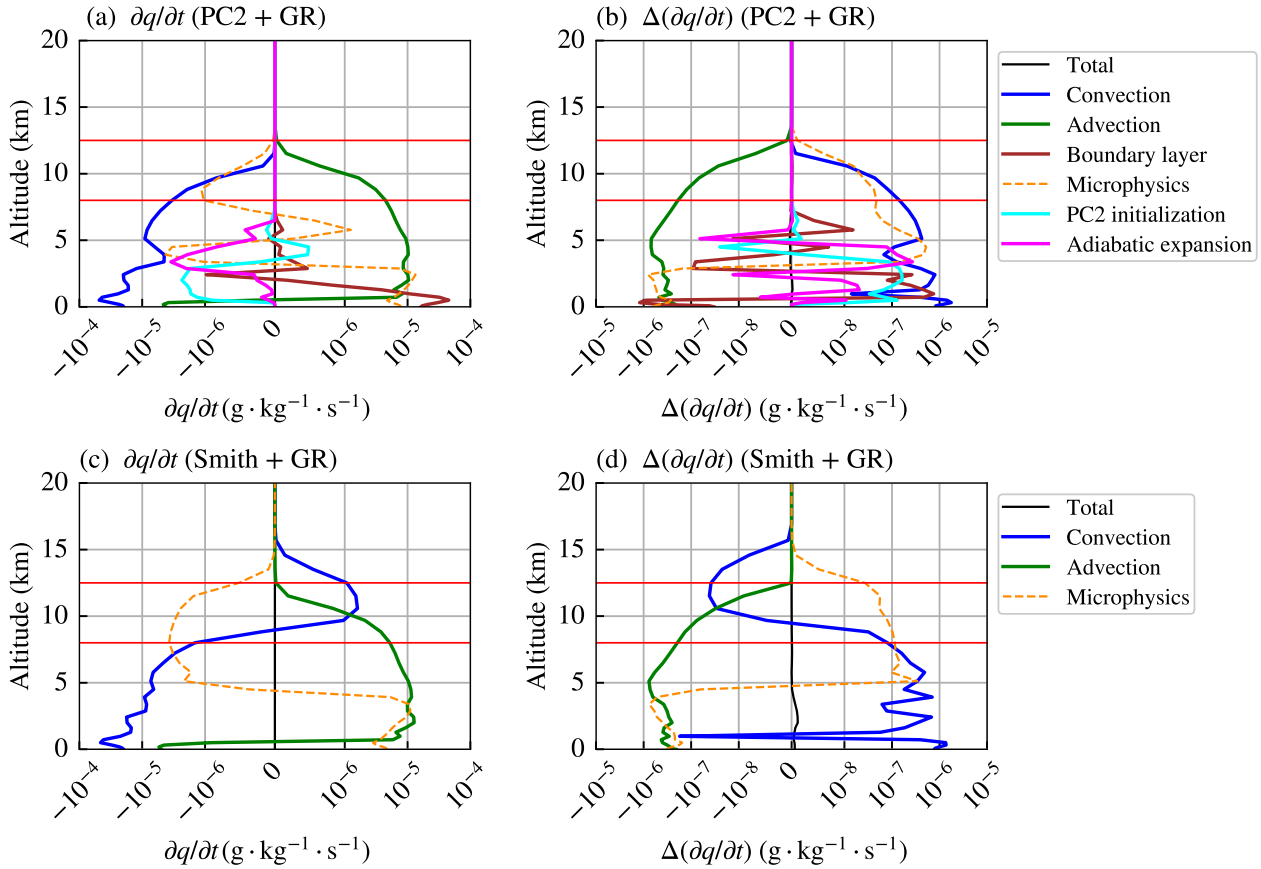

Figure S8. Vertical profiles of specific humidity tendencies in the control simulation (a, c) and their responses to extratropical warming (b, d) are plotted for both the prognostic (a, b) and diagnostic cloud schemes (c, d). A decrease in the advective tendency of specific humidity can be observed for both the cloud schemes (green curves), leading to reduced water vapor in the upper troposphere of the tropical ascent region. Note that the convectively detrained cloud condensates are evaporated in the diagnostic (Smith) cloud scheme resulting in a convective source of water vapor in the deep tropical upper troposphere (blue curve in (c)).

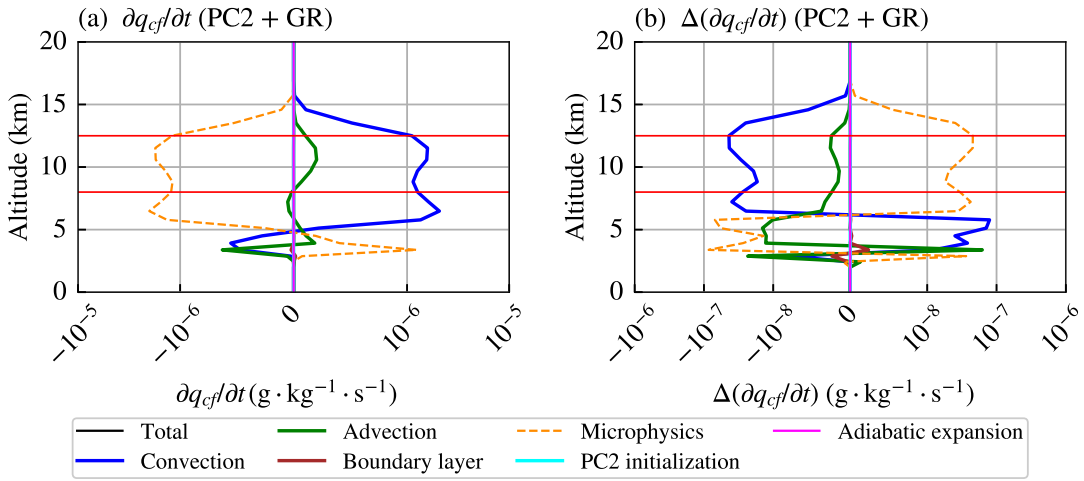

Figure S9. Vertical profiles of the tendencies of mass fraction of ice cloud condensates in the control simulation (a) and their responses to extratropical warming (b) are plotted for the PC2 (prognostic) cloud scheme with the GR mass-flux convection scheme. A decrease in the convective tendency of q_{cf} corresponds to a decrease in the updraft mass flux (M) in the tropical ascent region. The decrease in the microphysical tendency of ice cloud condensates (orange dashed curve in (b)) corresponds to a decrease in the sedimentation sink of ice aggregates, owing to the decrease in ice cloud fraction with extratropical warming.

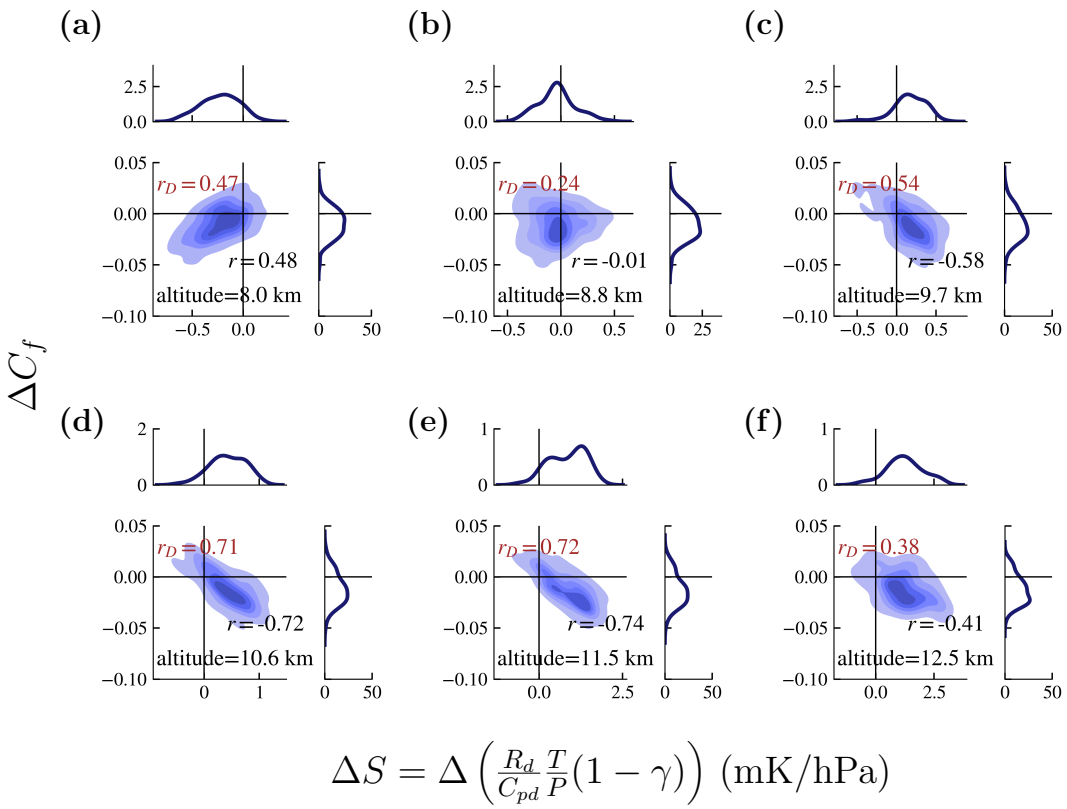

Figure S10. Kernel density estimates for the joint probability density function of changes in ice cloud fraction (ΔC_f) and dry static stability (ΔS), where $S = \frac{R_d}{C_{pd}}\frac{T}{P}(1-\gamma)$, are presented. The zonal- and annual means of the respective quantities are plotted, and the Pearson (r) and distance correlation coefficient (r_D) are computed. The figure shows an increase in the dry static stability with altitude as a result of extratropical warming, albeit the altitude at which clouds detrain remaining relatively unchanged in the perturbed simulations. Note that the changes in the dry static stability are dominated by the changes in $(1-\gamma)$ as shown in figure S11.

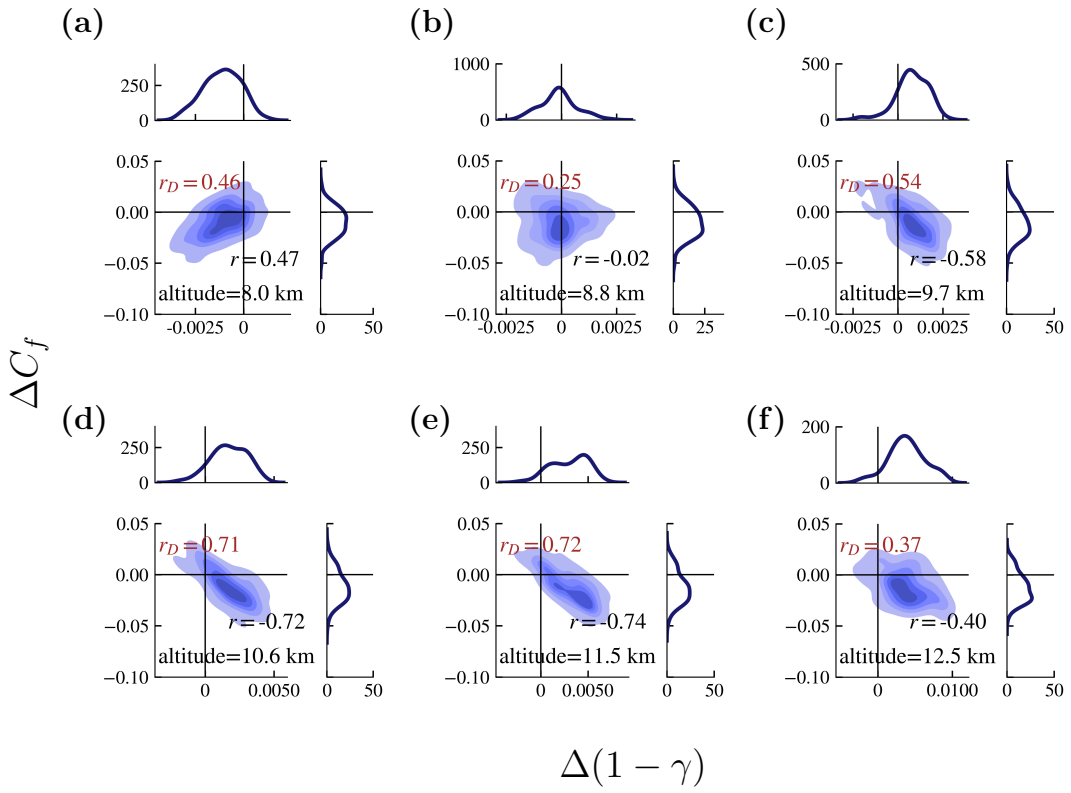

Figure S11. Kernel density estimates for the joint probability density function of changes in ice cloud fraction and $(1-\gamma)$ are presented. Here, $\gamma = \Gamma/\Gamma_d$ is the ratio of the moist to the dry adiabatic lapse rates. The zonal- and annual means of the respective quantities are plotted, and the Pearson (r) and distance correlation coefficient (r_D) are computed. The increase in static stability with altitude corresponds to an increase in $(1-\gamma)$ or a decrease in the moist adiabatic lapse rate $(\Gamma = -(\partial T/\partial z))$.

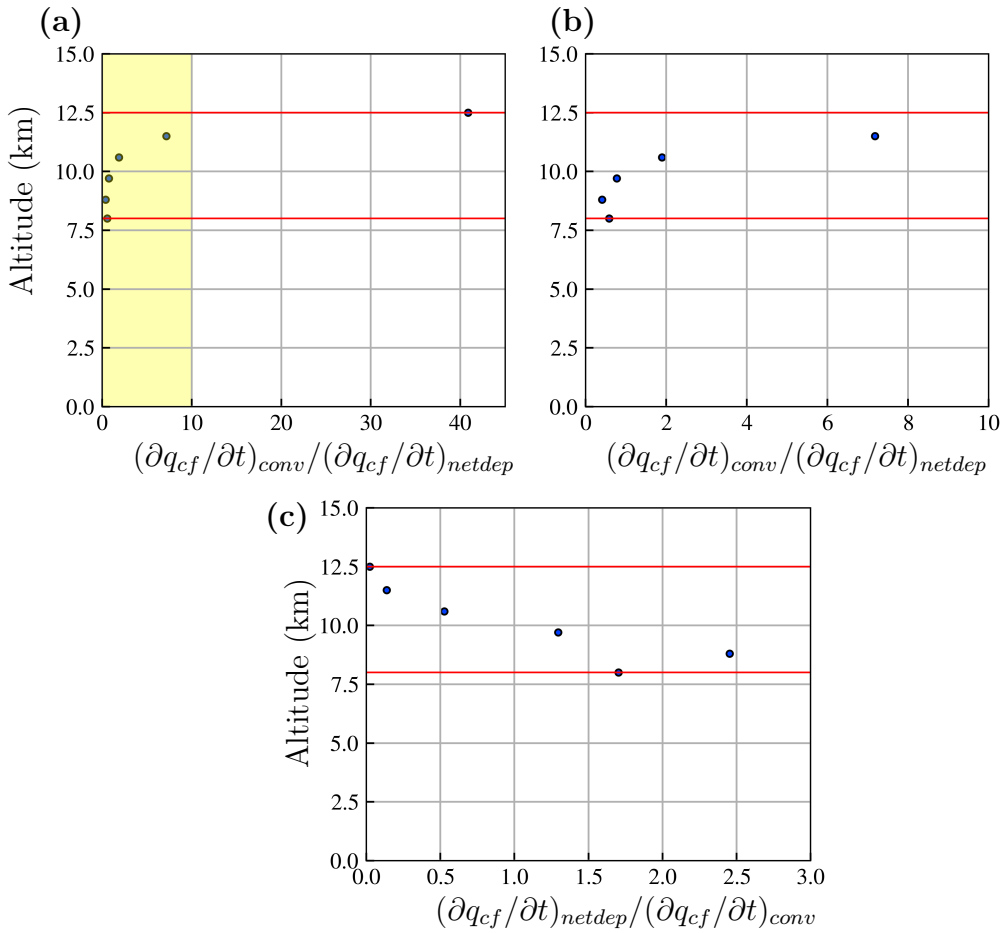

Figure S12. Ratio (a,b) and inverse ratio (c) of the convective tendency of mass fraction of cloud ice ($(\frac{\partial q_{cf}}{\partial t})_{conv}$) to its net depositional tendency ($((\frac{\partial q_{cf}}{\partial t})_{netdep}$) are plotted. The subfigure (a) shows the leading-order influence of net convective detrainment in controlling ice cloud condensates and therefore ice cloud fraction near the peak net detrainment region (above 10 km). The shaded portion (in yellow) in subfigure (a) is shown on a different horizontal scale in (b), and along with subfigure (c) clearly depicts the importance of net depositional growth of ice cloud condensates over its convective tendency between the altitude range of 8 to 10 km. Annual and zonal-mean quantities averaged over the tropical ascent region over a period of 15 simulation years are plotted.